



Antibonding Induced Anharmonicity Leading to Ultralow Lattice Thermal Conductivity and Extraordinary Thermoelectric Performance in CsK₂X (X = Sb, Bi)

Journal:	<i>Journal of Materials Chemistry C</i>
Manuscript ID	TC-ART-08-2022-003356.R1
Article Type:	Paper
Date Submitted by the Author:	18-Sep-2022
Complete List of Authors:	Yuan, Kunpeng; Dalian University of Technology, Zhang, Xiaoliang; Dalian University of Technology, School of Energy and Power Engineering Chang, Zheng; Dalian University of Technology, School of Energy and Power Engineering Tang, Dawei; Dalian University of Technology, School of Energy and Power Engineering Hu, Ming; University of South Carolina, Mechanical Engineering

Antibonding Induced Anharmonicity Leading to Ultralow Lattice Thermal Conductivity and Extraordinary Thermoelectric Performance in CsK₂X (X = Sb, Bi)

Kunpeng Yuan¹, Xiaoliang Zhang^{1*}, Zheng Chang¹, Dawei Tang^{1*}, and Ming Hu^{2*}

¹Key Laboratory of Ocean Energy Utilization and Energy Conservation of Ministry of Education, School of Energy and Power Engineering, Dalian University of Technology, Dalian 116024, China.

²Department of Mechanical Engineering, University of South Carolina, Columbia, 29208, USA

*Corresponding author. zhangxiaoliang@dlut.edu.cn (X.Z.); dwtang@dlut.edu.cn (D.T.); hu@sc.edu (M.H.)

ABSTRACT

Full Heusler compounds have long been discovered as exceptional *n*-type thermoelectric materials. However, no *p*-type compounds could match the high *n*-type figure of merit (*ZT*). In this work, based on first-principles transport theory, we predict the unprecedentedly high *p*-type *ZT* = 2.2 at 300 K and 5.3 at 800 K in full Heusler CsK₂Bi and CsK₂Sb, respectively. By incorporating the higher-order phonon scattering, we find that the high *ZT* value primarily stems from the ultralow lattice thermal conductivity (κ_L) of less than 0.2 W/mK at room temperature, decreased by 40% compared to the calculation only considering three-phonon scattering. Such ultralow κ_L is rooted in the enhanced phonon anharmonicity and scattering channels stemming from the coexistence of antibonding-induced anharmonic rattling of Cs atoms and low-lying optical branches. Moreover, the flat and heavy nature of valence band edges leads to a high Seebeck coefficient and moderate power factor at optimal hole concentration, while the dispersive and light conduction band edges yield much larger electrical conductivity and electronic thermal conductivity (κ_e), and the predominant role of κ_e suppresses the *n*-type *ZT*. This study offers a deeper insight into the thermal and electronic transport properties in full Heusler compounds with strong phonon anharmonicity and excellent thermoelectric performance.

1. INTRODUCTION

Improving the energy utilization efficiency can not only satisfy the ever-increasing demand for energy, but also tackle the climate crisis by reducing carbon emissions. Thermoelectric materials that can generate electricity from waste heat have been paid extensive attention as promising candidates for sustainable and environmentally friendly energy conversion technologies.¹⁻³ However, the low thermoelectric conversion efficiency impedes the large-scale commercial applications of the thermoelectric device. The conversion efficiency of thermoelectric materials is primarily characterized by the dimensionless figure of merit $ZT = S^2\sigma T/\kappa$, where S is the Seebeck coefficient, σ is the electrical conductivity, T is the absolute temperature, and κ is the thermal conductivity consisting of electronic and lattice contributions. As we can see, enhancing ZT can be achieved either by maximizing the power factor ($PF = S^2\sigma$) or by minimizing the thermal conductivity. Unfortunately, the requirements of band structure for high S and σ are reversed. On the other hand, the increase of σ will lead to a larger electronic contribution to the thermal conductivity according to $\kappa_e = L\sigma T$, where L is the Lorenz number. These interdependent properties leave a key challenge to decouple the electronic and thermal transport properties.⁴

Since the lattice thermal conductivity is relatively independent of the electronic transport properties, seeking the material with intrinsically low lattice thermal conductivity has been paid many efforts in the past decades. It has been demonstrated that the underlying mechanisms driving low lattice thermal conductivity are associated closely with lattice anharmonicity.⁵⁻⁷ Several strategies are found to trigger strong anharmonicity, such as stereochemically active lone-pair electrons,^{8,9} resonant bonding,^{10,11} and rattling atoms.¹²⁻¹⁴ Among these, the rattling model offers a rich playground for lowering the lattice thermal conductivity by tuning the vast structural and chemical space. The rattling behavior refers to the large amplitude vibrations of weakly bound atoms or atom clusters, resulting in the softening of the acoustic phonon branches owing to the avoided crossing effect. This characteristic was first found in host-guest framework structures such as clathrates^{15,16} and partially filled skutterudites.^{17,18} Recently, some descriptors have been proposed to screen the materials with intrinsic rattling atoms. Liu et al. found that the crystallographic site occupancy factor could be an effective indicator to

identify a material with low lattice thermal conductivity.¹⁹ They demonstrated that the atomic partial occupancy could lead to the anharmonic rattling vibration and atomic migration, which induce large anharmonicity and weak bonding environment. However, the crystallographic site occupancy factor can not fully describe the materials with intrinsic rattling atoms since many materials with atomic sites being fully occupied also have rattling atoms due to the weak interaction with the neighboring atoms. By analyzing the structural features of materials with the rattling model, Li et al. extracted a structural descriptor of the rattling atoms.¹⁴ If the distances between the specific atom and the nearest neighboring atoms are larger than the sum of corresponding covalent radiuses, the atom can vibrate like rattling. Many materials with intrinsic rattling atoms have been explored by this structural descriptor. Furthermore, prominent materials with intrinsic rattling atoms have been experimentally identified to exhibit low lattice thermal conductivity.²⁰⁻²²

Full Heusler compounds are a rare class of thermoelectric materials with the coexistence of high power factor and ultralow lattice thermal conductivity. He et al. reported the ultralow thermal conductivity in semiconducting full Heusler compounds with ten valence electrons through first-principles high-throughput screening.²³ Among these compounds, Ba₂AuBi exhibits the lowest lattice thermal conductivity (0.47 W/mK at 300 K) due to the strong anharmonic rattling of Au atoms. Based on a rigorous treatment of electron-phonon scattering, the optimal ZT values for n - and p -type Ba₂AuBi are as high as 5 and 2 at 800 K.^{24,25} Meanwhile, another full Heusler compound Sr₂BiAu was predicted to deliver n -type $ZT = 0.4\sim 4.9$ at $T = 100\sim 700$ K.²⁶ As we can see, the advanced full Heusler thermoelectric materials have the potential to achieve unprecedentedly high ZT for n -type doping compared to their p -type counterpart. The mismatch between the n - and p -type legs of the thermoelectric module would lead to the sacrifice of the conversion efficiency to some extent.

In this work, we predict the ultralow lattice thermal conductivity in full Heusler CsK₂X ($X = \text{Sb, Bi}$), which is even lower than previous reported full Heusler materials. The antibonding-induced anharmonic rattling of Cs atoms is found to trigger high-order phonon interactions, which strongly suppresses the contributions of the heat-carrying acoustic phonons to thermal transport. Additionally, the presence of low-frequency optical modes arising from the vibrations of Sb/Bi atoms enables more available phonon scattering channels. These two factors acting

together lead to the ultralow lattice thermal conductivity in CsK₂X (X = Sb, Bi). On the other hand, the flat valence band edges of CsK₂Sb yield much larger *p*-type power factor at the optimal carrier concentration compared to its *n*-type counterpart. The coexistence of low thermal conductivity and high *p*-type power factor results in an unprecedentedly high *p*-type $ZT = 5.3$ at 800 K.

2. COMPUTATIONAL DETAILS

All the first-principles calculations are carried out based on density functional theory (DFT) as implemented in the Vienna ab-initio Simulation Package (VASP).²⁷ The projector-augmented wave (PAW) pseudopotentials are used to describe the interaction among atoms and the generalized gradient approximation (GGA) in the Perdew-Burke-Ernzerhof (PBE) form is chosen as the exchange-correlation functional.^{28,29} The kinetic energy cutoff of the plane-wave function is set to 600 eV for all the calculations. The convergent criterion for the total energy difference between two successive self-consistency steps is 10⁻⁸ eV and the primitive cell is fully relaxed until the maximum force acting on each atom is less than 10⁻⁸ eV/Å. A well-converged Γ -centered **k**-point grid of 10×10×10 is used to sample the first irreducible Brillouin zone.

In this work, moment tensor potential (MTP) is trained to evaluate the phonon transport properties using the MLIP package.³⁰ The training set for the development of MTP is prepared by DFT calculations and active learning is used to automatically refine the training set. First, ab initio molecular dynamics (AIMD) simulations of 3×3×3 supercell and Γ -point sampling are performed in the temperature range from 100 to 800 K with an interval of 100 K. The total simulation time is 1 ps with a timestep of 1 fs. For each run, 50 configurations are selected from the last 0.5 ps (one configuration is sampled every 10 time steps) and the initial training sets include 400 configurations in total. To evaluate the energy and force more accurately, the initial configurations are recalculated with the Γ -centered **k**-point grid of 2×2×2. Then, the first MTP model can be trained on the initial 400 configurations and molecular dynamics (MD) simulations of 3×3×3 supercell in the same temperature range as the AIMD are performed using LAMMPS.³¹ The configurations whose extrapolation grade exceeds the threshold are added to the preselected set, then some of them are selected with MaxVol algorithm. Finally, energies,

forces, and stresses of the selected configurations are calculated by DFT and added to the training set. After that, the MTP can be retrained and the process is repeated until the chosen threshold is satisfied. With the help of active learning process, 780 and 896 configurations for CsK₂Sb and CsK₂Bi are selected to train the final MTP. The cutoff radius of our MTP model is set to 9.5 Å for both CsK₂Sb and CsK₂Bi. The maximum level is equal to 18 to define the particular functional form of MTP. The accuracy of our trained MTP model can be found in the Supporting Information.

The lattice thermal conductivity and related phonon properties are calculated by iteratively solving the phonon Boltzmann transport equation (BTE) with the inputs of second-order (harmonic) and third-order (anharmonic) interatomic force constants (IFCs). The lattice thermal conductivity is given by

$$\kappa_L = \frac{1}{N_{\mathbf{q}} V k_B T^2} \sum_{\lambda} (\hbar \omega_{\lambda})^2 \mathbf{v}_{\lambda}^2 \tau_{\lambda} n_{\lambda} (n_{\lambda} + 1) \quad (1)$$

where $N_{\mathbf{q}}$ is the number of \mathbf{q} points in the first Brillouin zone, V is the volume of the unit cell, k_B is the Boltzmann constant, T is the absolute temperature, \hbar is the reduced Planck constant, ω and \mathbf{v} are the frequency and group velocity of phonon mode, τ is the phonon lifetime, n is the equilibrium Bose-Einstein distribution function, λ represents phonon mode with wave vector \mathbf{q} and polarization ν .

In order to assess the effect of temperature on phonon renormalization, the temperature-dependent effective potential method implemented in the Hiphive package³² was employed to obtain the effective IFCs. We performed classical MD simulations on 4×4×4 supercell with MTP using LAMMPS at different temperatures from 300 K to 800 K with the interval of 100 K. For each temperature, we selected 100 configurations every 100 timesteps in the production run with NVE ensemble, then the corresponding atomic forces were used to fit the force constants. Figures S1 and S2 show the root mean square errors of atomic forces for different second-, third-, and fourth-order cutoff distances. After the convergence test, the second-, third-, and fourth-order IFCs cutoff distances were set to 9.0, 8.0, and 5.0 Å for both CsK₂Sb and CsK₂Bi. ShengBTE package³³ was used to calculate the lattice thermal conductivity with 15×15×15 \mathbf{q} -grid by balancing the computational cost and accuracy. The effects of long-range electrostatic interactions are incorporated into the dynamic matrix based on the Born effective

charges and dielectric constants.

We also carried out phonon spectral energy density (SED) analysis,³⁴ which includes all high-order phonon interactions. The phonon normal modes and SED are obtained by³⁵

$$\mathcal{G}(\mathbf{q}, \nu, t) = \sum_{jl} \sqrt{\frac{m_j}{N}} \mathbf{v}_{jl}(t) \mathbf{e}_j(\mathbf{q}, \nu) \exp(-2\pi i \mathbf{q} \cdot \mathbf{r}_l) \quad (2)$$

$$\Phi(\mathbf{q}, \nu, \omega) = \left| \int \mathcal{G}(\mathbf{q}, \nu, t) \exp(-i\omega t) dt \right|^2 \quad (3)$$

Where m_j is mass of the j th atom, N is the number of unit cells, \mathbf{v}_{jl} is the velocity of the j th atom located inside the l th unit cell (\mathbf{r}_l), and $\mathbf{e}_j(\mathbf{q}, \nu)$ is the eigenvector of the phonon mode. The atomic velocities were obtained from equilibrium MD simulations in the NVE ensemble using MTP. To be consistent with the \mathbf{q} -grid applied in the BTE method, a $15 \times 15 \times 15$ supercell (13500 atoms) was used to perform the MD simulations and three independent runs were carried out to obtain the average SED. The phonon lifetime can be obtained by fitting the SED peak with the Lorentzian function³⁶

$$\Phi(\mathbf{q}, \nu, \omega) = \frac{I}{1 + \left(\frac{\omega - \omega_0}{\Gamma} \right)^2} \quad (4)$$

where I is the peak magnitude, ω is the frequency at the peak center, and Γ is the half width at half maximum. The phonon lifetime is defined as $\tau = 1/(2\Gamma)$. Once the phonon lifetime is obtained, the lattice thermal conductivity can be calculated using Eq. (1).

The electronic transport properties in these two materials are calculated using the AMSET package³⁷ based on the electron Boltzmann transport equation. The PBE functional was used to calculate the electronic band structure. The uniform non-self-consistent calculations used as input of the electronic transport calculations were run with $12 \times 12 \times 12$ \mathbf{k} -grid, and a finer $75 \times 75 \times 75$ \mathbf{k} -grid was used to interpolate band structure in order to get convergent results. The Heyd-Scuseria-Ernzerhof (HSE06) hybrid functional was used to correct the band gap using a scissor operation. Spin-orbit interactions were included for both materials.

For electrical transport properties, the Seebeck coefficient, electrical conductivity, and electronic thermal conductivity are calculated as

$$S_{\alpha\beta}(T, \mu) = \frac{1}{eTV\sigma_{\alpha\beta}(T, \mu)} \int_{-\infty}^{+\infty} \sum_{\alpha\beta}(\varepsilon) (\varepsilon - \mu) \left[-\frac{\partial f(T, \varepsilon, \mu)}{\partial \varepsilon} \right] d\varepsilon \quad (5)$$

$$\sigma_{\alpha\beta}(T, \mu) = \frac{1}{V} \int_{-\infty}^{+\infty} \sum_{\alpha\beta}(\varepsilon) \left[-\frac{\partial f(T, \varepsilon, \mu)}{\partial \varepsilon} \right] d\varepsilon \quad (6)$$

$$\kappa_{e,\alpha\beta}(T, \mu) = \frac{1}{TV} \int_{-\infty}^{+\infty} \sum_{\alpha\beta}(\varepsilon) (\varepsilon - \mu)^2 \left[-\frac{\partial f(T, \varepsilon, \mu)}{\partial \varepsilon} \right] d\varepsilon - TS_{\alpha\beta}^2(T, \mu) \sigma_{\alpha\beta}(T, \mu) \quad (7)$$

where μ is chemical potential, ε is the band energy, f is the Fermi-Dirac distribution function of carriers, $\sum_{\alpha\beta}(\varepsilon)$ is the transport distribution function and defined as

$$\sum_{\alpha\beta}(\varepsilon) = \frac{e^2}{N_{\mathbf{k}}} \sum_{i,\mathbf{k}} \tau_{e,i\mathbf{k}} v_{e,i\mathbf{k}}^{\alpha} v_{e,i\mathbf{k}}^{\beta} \delta(\varepsilon - \varepsilon_{i\mathbf{k}}) \quad (8)$$

where the summation is over all bands i and over all \mathbf{k} grid, τ_e is the electronic relaxation time, v_e is the electronic group velocity.

As the key parameters, the mode-dependent carrier scattering rates are treated by the momentum relaxation time approximation, and the probability of scattering from initial state $\psi_{i\mathbf{k}}$ to final state $\psi_{m\mathbf{k}+\mathbf{q}}$ can be calculated through Fermi's golden rule as

$$\tau_{i\mathbf{k} \rightarrow m\mathbf{k}+\mathbf{q}}^{-1} = \frac{2\pi}{\hbar} |g_{im}(\mathbf{k}, \mathbf{q})|^2 \delta(\varepsilon_{i\mathbf{k}} - \varepsilon_{m\mathbf{k}+\mathbf{q}}) \quad (9)$$

where $g_{im}(\mathbf{k}, \mathbf{q})$ is the electron-phonon coupling matrix and informs the transition of an electron from initial state $\psi_{i\mathbf{k}}$ with band i and wave vector \mathbf{q} to final state $\psi_{m\mathbf{k}+\mathbf{q}}$ with band m and wave vector $\mathbf{k} + \mathbf{q}$, and $\varepsilon_{i\mathbf{k}}$ is the energy of state $\psi_{i\mathbf{k}}$. In this work, the acoustic deformation potential scattering (AD), polar optical phonon scattering (PO), and ionized impurities (IM) are considered to contribute to the carrier scattering rates. More details are included in the Supplemental Information.

3. RESULTS AND DISCUSSION

Full Heusler compounds CsK_2X ($\text{X} = \text{Sb}, \text{Bi}$) have face-centered cubic crystal structure with space group $Fm\bar{3}m$ (No. 225). The conventional and primitive cells are shown in Figure 1(a-b). The K atoms form a simple cubic sublattice, the Cs and X atoms are orderly arranged within body centers in the CsCl-type structure. The fully relaxed lattice constants of CsK_2X ($\text{X} = \text{Sb}, \text{Bi}$) are 8.76 and 8.94 Å, respectively, which are in agreement with previous DFT results.³⁸⁻⁴⁰

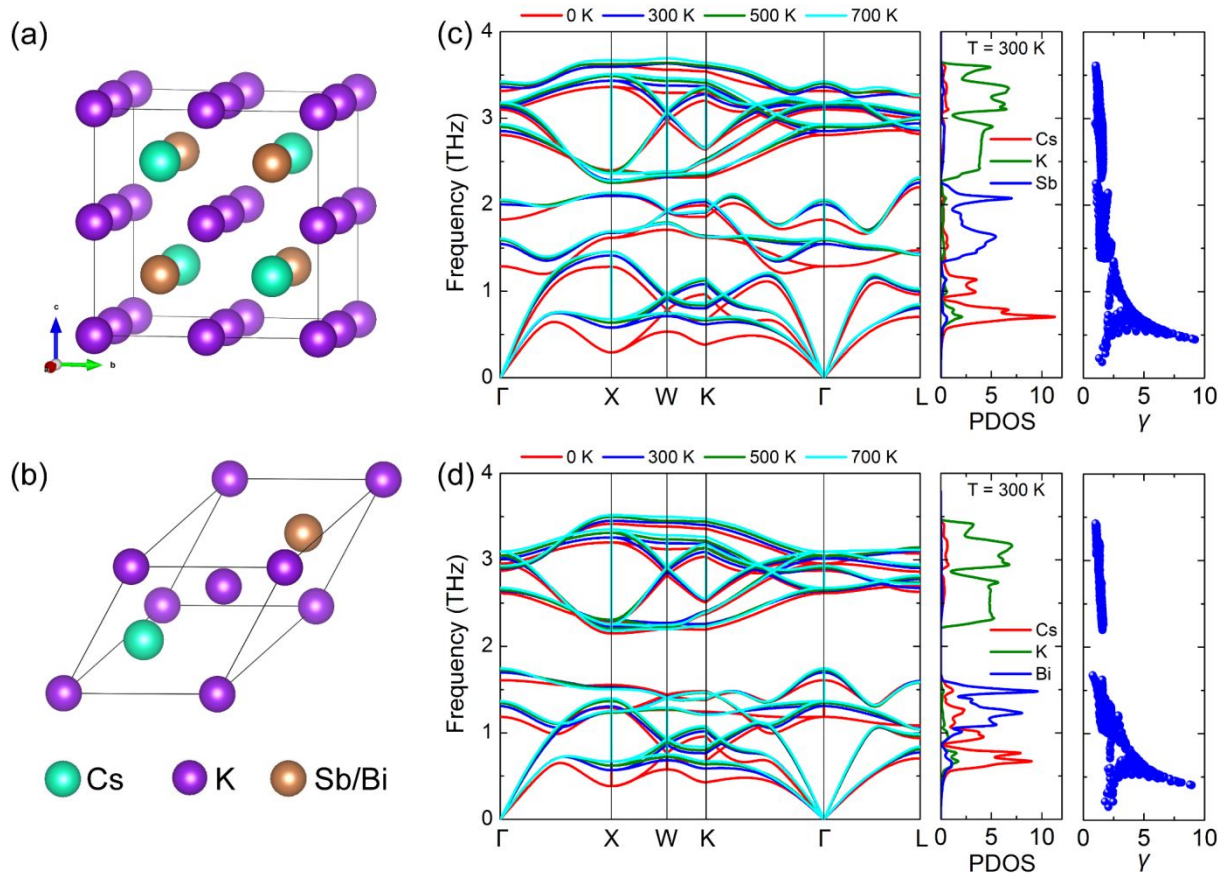


Figure 1. (a) Conventional and (b) primitive cell of full Heusler compounds CsK_2X ($\text{X} = \text{Sb}, \text{Bi}$). Temperature-dependent phonon dispersions, atom-decomposed phonon density of states (PDOS) at 300K, and mode Grüneisen parameters (γ) of (c) CsK_2Sb and (d) CsK_2Bi .

More insights into the rattling vibrations are provided by lattice dynamics properties. It is well known that the phonon frequencies of rattler modes are very sensitive to the temperature and exhibit strong renormalization effects. Figure 1(c-d) displays the temperature-dependent phonon dispersions and the corresponding atom-decomposed phonon density of states (PDOS). It can be seen that the calculated phonon dispersion exhibits three distinct regions. As indicated in the PDOS, the acoustic modes are dominated by the Cs atoms. In contrast, the low- and high-frequency optical modes are contributed by the Sb/Bi and K atoms, respectively.

The presence of an avoided crossing between the longitudinal acoustic branches and low-frequency optical branches along the Γ -X, Γ -K, and Γ -L directions is a significant characteristic of the Cs atoms acting as rattlers. The effect of avoided crossing is to lower the group velocity of the acoustic phonons, and thereby the lattice thermal conductivity, by flattening the bands. Another remarkable signature is the large atomic displacement parameter (ADP). ADP is a measure of the mean-square displacement of an atom about its equilibrium position. Our

analysis shows that Cs atoms possess larger atomic displacement parameters compared to K and Sb/Bi atoms (see Figure S3 in the Supporting Information), affirming their rattling behavior. The anharmonic rattling dynamics of Cs atoms are also found in Cs-containing vacancy-ordered double perovskites.⁴¹⁻⁴³

It can also be seen that the hardening of the phonon frequencies of rattling modes is significant, especially for acoustic modes at the zone boundary and low-frequency optical modes around the zone center. This obvious phonon renormalization indicates strong anharmonicity, which can severely suppress phonon transport. A quick evaluation of the anharmonicity is made by the mode specific Grüneisen parameters as presented in the right panel of Figure 1(c-d). The Grüneisen parameters of acoustic modes and low-frequency optical modes are obviously larger than other phonon modes, supporting the results of renormalized phonon dispersions.

Having established a solid picture of lattice dynamics properties, we proceed to investigate the lattice thermal conductivity κ_L , which is a key ingredient in the field of thermoelectricity. Figure 2 compares lattice thermal conductivity κ_L based on BTE and SED, respectively. For the BTE method, temperature-renormalized IFCs and scattering processes up to three-phonon interactions (the lowest-order perturbation of cubic anharmonicities) and four-phonon interactions are considered. The calculated room-temperature lattice thermal conductivities based on the BTE method with only three-phonon scattering are 0.27 and 0.23 W/mK for CsK₂Sb and CsK₂Bi, respectively. The κ_L of CsK₂Bi is slightly lower than that of CsK₂Sb due to the heavier Bi atom and smaller group velocity. It is well known that higher-order phonon interactions cannot be ignored for strongly anharmonic materials. After including four-phonon scattering, the κ_L based on BTE reduce to 0.15 and 0.14 W/mK at 300 K for CsK₂Sb and CsK₂Bi, respectively. We also calculate the lattice thermal conductivity based on the SED method, which includes all high-order phonon interactions. We find that the lattice thermal conductivities are largely suppressed due to higher-order interactions and the values of SED κ_L are 0.14 and 0.13 W/mK at 300 K for CsK₂Sb and CsK₂Bi, respectively. Specifically, the κ_L is decreased by as large as 48% and 43% for CsK₂Sb and CsK₂Bi compared to three-phonon scattering. Our work shows that the phonon heat transport in CsK₂Sb and CsK₂Bi is hindered by higher-order phonon interactions and both materials exhibit ultralow lattice thermal

conductivities, which are comparable to or lower than previous reported values in other thermoelectric materials, such as TlInTe_2 (~ 0.46 W/mK at 300 K),¹³ TlCuSe (~ 0.44 W/mK at 300 K),⁴⁴ and Cs_2SnI_6 (~ 0.29 W/mK at 300 K).⁴² Moreover, previous work found that the full Heusler Ba_2AuBi has low κ_L (0.45 W/mK at 300 K) based on BTE and the lowest-order perturbation of cubic anharmonicities.²³ Even without considering higher-order anharmonicities, our BTE results for CsK_2Sb and CsK_2Bi are even lower than that of Ba_2AuBi .

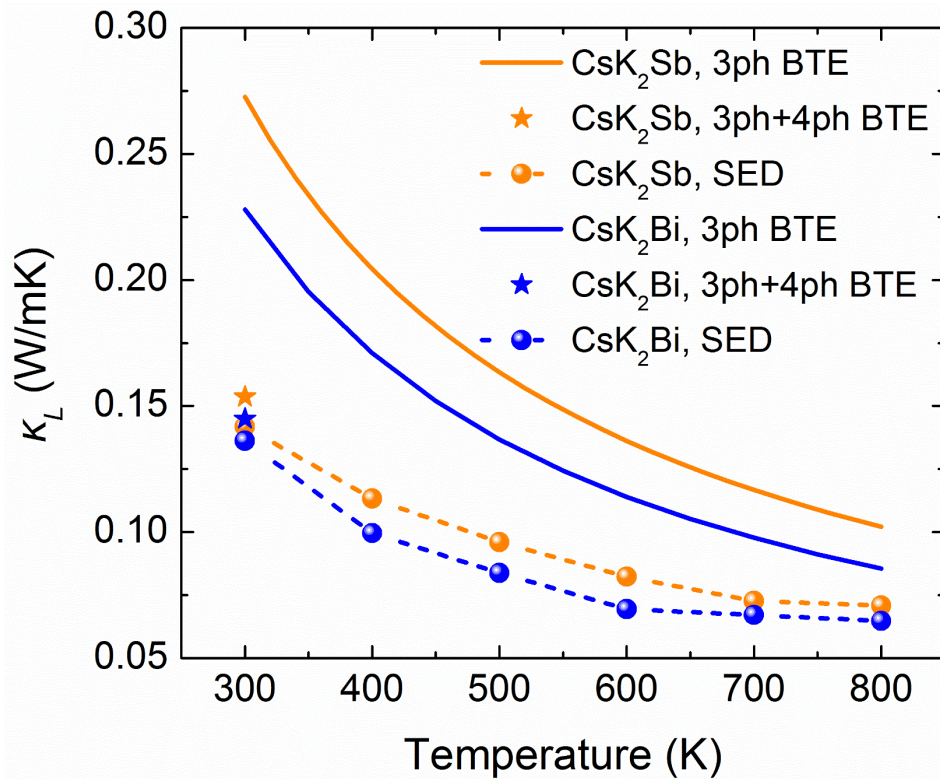


Figure 2. Temperature-dependent lattice thermal conductivity (κ_L) calculated from BTE considering only three-phonon (3ph) scattering and after including four-phonon (3ph+4ph) scattering, and from SED including all high-order phonon scattering.

Furthermore, frequency-dependent thermal conductivity and phonon scattering rate are given in Figure 3 to clarify the microscopic mechanisms of ultralow thermal conductivity. From the spectrally decomposed lattice thermal conductivity $\kappa_L(\omega)$, we find that the acoustic phonon modes below 1 THz have the largest contributions to κ_L . When higher-order phonon interactions are considered, the $\kappa_L(\omega)$ of rattle-like acoustic phonon modes and optical phonon modes exhibits a reduction, which is confirmed by the pronounced increase in scattering rates for corresponding phonon modes shown in Figure 3(c-d). It is worth mentioning that the enhanced scattering rates spread over a wide range of frequencies rather than in a very limited range of frequencies for rattling modes. This behavior is consistent with prior findings, which

demonstrate that phonon scattering by rattlers is not resonant and the presence of low-frequency rattlers modes can significantly enhance phonon scattering phase space in a wide frequency range. To examine the effect of low-frequency phonon modes on scattering phase space, we further estimate the weighted phase space W , a measure of the allowed scattering channels that conserve both the energy and the momentum. As shown in Figure S4(a-b), by artificially reducing the atomic mass of Sb/Bi by a factor of three, we see that low-frequency optical modes move to higher frequencies. Figure S4(c-d) depicts the weighted three- and four-phonon scattering phase space based on the original and reduced atomic mass of Sb/Bi. It can be seen that the upward low-lying optical modes decrease the three- and four-phonon scattering phase space. Moreover, due to the upward of low-frequency optical modes, the allowed four-phonon scattering phase space is restricted over a wide frequency range. Thus, it presents a consistent picture with the results of scattering rates that the significant enhancement of phonon scattering rates over a wide frequency range by including higher-order interactions is attributed to the increase of the number of multi-phonon scattering channels due to the appearance of low-lying phonon modes.

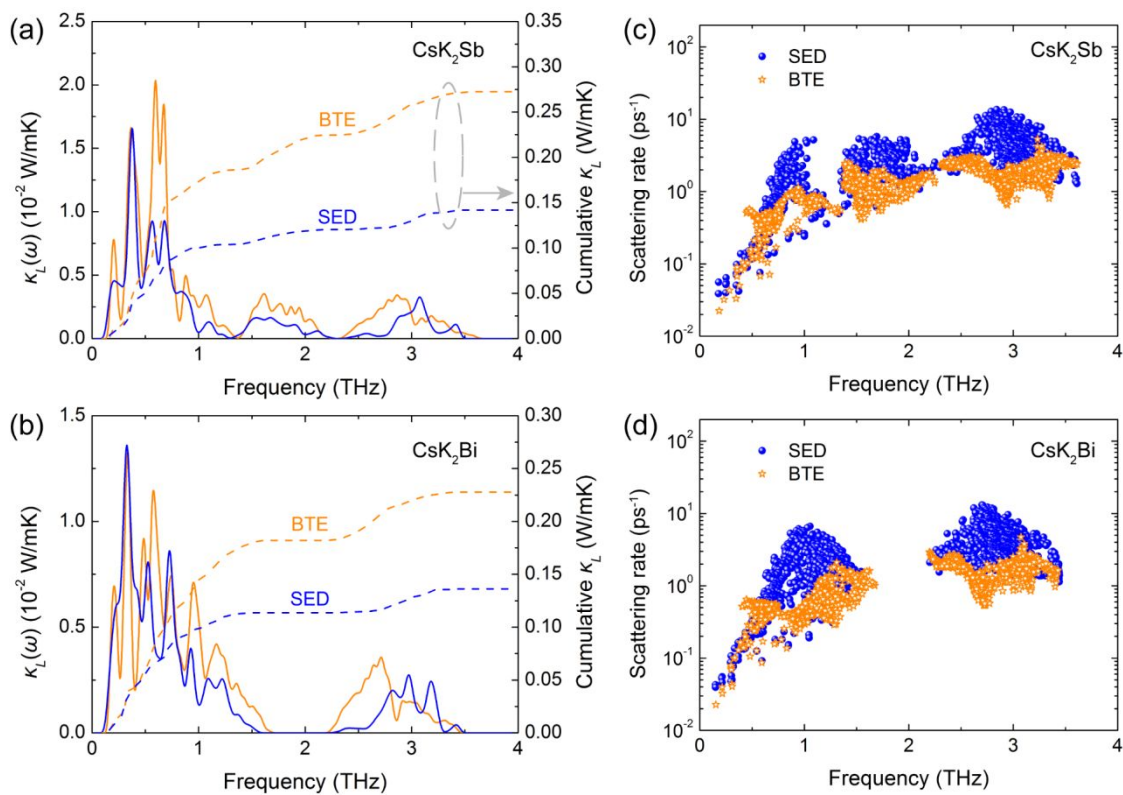


Figure 3. Room-temperature lattice thermal conductivity spectrum $\kappa_L(\omega)$ and its cumulative values of (a) CsK₂Sb and (b) CsK₂Bi. Phonon mode-resolved scattering rates of (c) CsK₂Sb and (d) CsK₂Bi calculated from BTE and SED at 300 K.

The calculated band structure and atom projected density of states (DOS) of CsK₂Sb and CsK₂Bi are shown in Figures S5 and S6. The calculated band gap of CsK₂Sb based on PBE exchange functional including SOC is 0.70 eV, while the corresponding band gap of CsK₂Bi is zero. To overcome the common underestimation of band gap using the PBE exchange functional, the HSE06 functional is adopted, yielding a larger band gap of 1.21 eV and 0.22 eV for CsK₂Sb and CsK₂Bi, respectively. Photoconductivity measurements yielded a similar gap of 1.2 eV for CsK₂Sb.⁴⁵ Both CsK₂Sb and CsK₂Bi are direct band-gap semiconductors, and the valence band maximum (VBM) and the conduction band minimum (CBM) locate at the Γ point. A distinguishing feature between the valence band and the conduction band is that the conduction band is more dispersive than the valence band. The principal effective masses for holes at the Γ point are $6.23 m_e$ and $3.64 m_e$ for CsK₂Sb and CsK₂Bi, while the effective masses for electrons at the Γ point are $6.23 m_e$ and $3.64 m_e$ for CsK₂Sb and CsK₂Bi. The valence band edge is dominated by Sb/Bi p orbitals (see Figures S7 and S8 in the Supporting Information) and its flat nature leads to heavy hole effective mass and a sharp increase in the density of states, which is beneficial to the enhancement of the Seebeck coefficient. In contrast, the conduction band edge has hybridized sp character and the dispersive band results in low electron effective mass, which is indicative of high electron mobility and electrical conductivity.

The carrier mobility of CsK₂Sb and CsK₂Bi limited by different scattering mechanisms is displayed in Figure 4 and Figure S9. The trend of carrier mobility against temperature is found to be mainly limited by polar optical phonon scattering, which is similar to other polar semiconductors.^{37, 46, 47} At low carrier concentrations, as the carrier concentration increases, the polar optical phonon scattering is still the most important factor limiting mobility. However, with the increase of carrier concentration, the polar optical phonon scattering is weakened by the increased screening from the extra carriers, in contrast, the ionized impurity scattering is enhanced due to a larger number of ionized impurities.^{48, 49} As a result, the ionized impurity scattering becomes the dominant mobility-limiting factor at high concentrations. For p -type doping CsK₂Sb, the turning point is around $1 \times 10^{20} \text{ cm}^{-3}$, while the crossover concentration for n -type doping is not shown in Figure 4(d), because it is out of the range where the maximum ZT occurs. In addition, the room-temperature electron mobility of CsK₂Sb can reach $422 \text{ cm}^2/\text{Vs}$ at $n_e = 1 \times 10^{19} \text{ cm}^{-3}$, for comparison, the corresponding hole mobility is only $10 \text{ cm}^2/\text{Vs}$

at $n_h = 1 \times 10^{19} \text{ cm}^{-3}$, which is one order of magnitude smaller than that of electron. A comparison of CsK₂Sb and CsK₂Bi gives higher carrier mobility for CsK₂Bi due to its smaller effective mass.

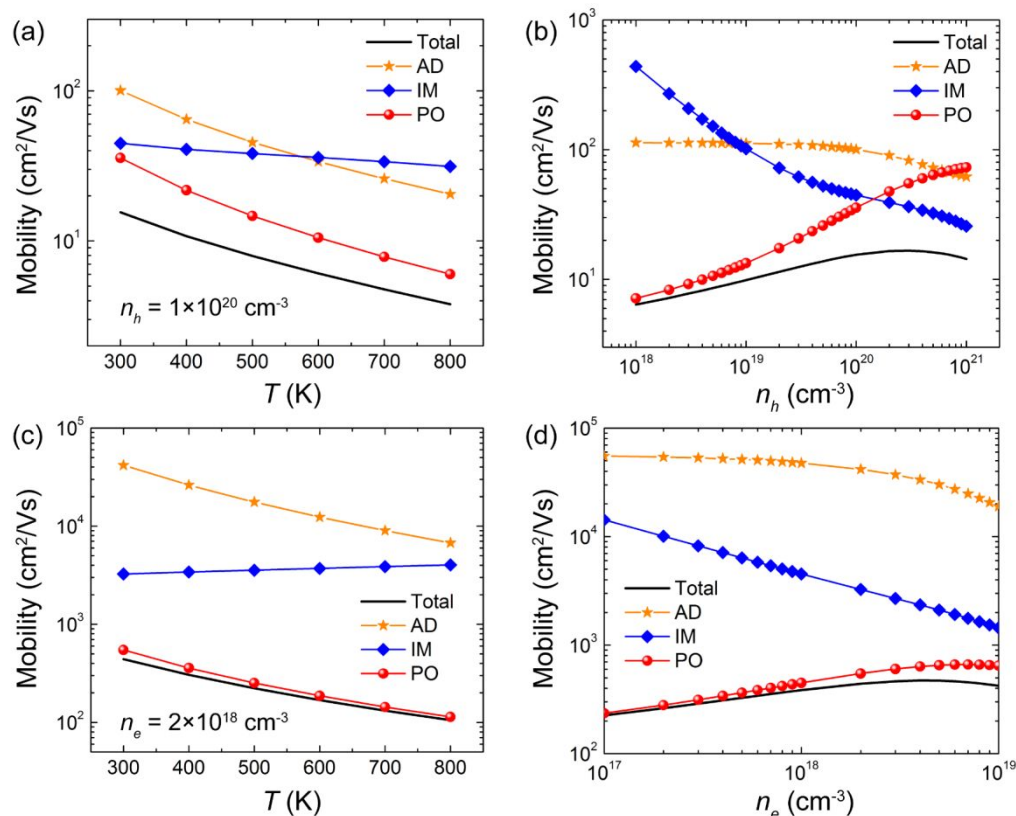


Figure 4. (a) Hole mobility of CsK₂Sb at a hole concentration of $1 \times 10^{20} \text{ cm}^{-3}$ as a function of temperature. (b) Room-temperature hole mobility of CsK₂Sb against hole concentration. (c) Electron mobility of CsK₂Sb at an electron concentration of $2 \times 10^{18} \text{ cm}^{-3}$ as a function of temperature. (d) Room-temperature electron mobility of CsK₂Sb against electron concentration. AD, IM, and PO represent the acoustic deformation potential scattering, ionized impurity scattering, and polar optical phonon scattering.

To evaluate the potential of CsK₂Sb and CsK₂Bi as a thermoelectric module, the electronic transport properties are shown in Figure 5 and Figure S10 as a function of carrier concentration. Owing to the superior thermoelectric performance of CsK₂Sb, we focus on the electronic transport properties of CsK₂Sb in the following text, the results of CsK₂Bi are discussed in the Supplemental Material. Since there is no significant change regarding the shape of band structure calculated by the PBE and HSE06 functionals, the PBE results are used for the electronic transport properties except that the band gap is corrected by the HSE06 functional. It can be seen that, at the same carrier concentration, the *p*-type Seebeck coefficient of CsK₂Sb is clearly much higher than the *n*-type counterpart, while the *p*-type electrical conductivity of CsK₂Sb is much lower than the *n*-type electrical conductivity. For instance, at a fixed carrier

concentration of $1 \times 10^{19} \text{ cm}^{-3}$, the room-temperature Seebeck coefficients are $450 \mu\text{V/K}$ for p -type and $-75 \mu\text{V/K}$ for n -type, while the room-temperature electrical conductivities are $2 \times 10^3 \text{ S/m}$ for p -type and $6 \times 10^4 \text{ S/m}$ for n -type. This is consistent with our previous analysis of band structure. In addition, we note that the electron contribution to the thermal conductivity can not be ignored at high concentrations. The room-temperature electronic thermal conductivity of CsK_2Sb becomes larger than the lattice thermal conductivity as the hole concentration exceeds $1 \times 10^{20} \text{ cm}^{-3}$. Due to the large n -type electrical conductivity, the total thermal conductivity is dominated by the electron contribution for $n_e > 3 \times 10^{18} \text{ cm}^{-3}$.

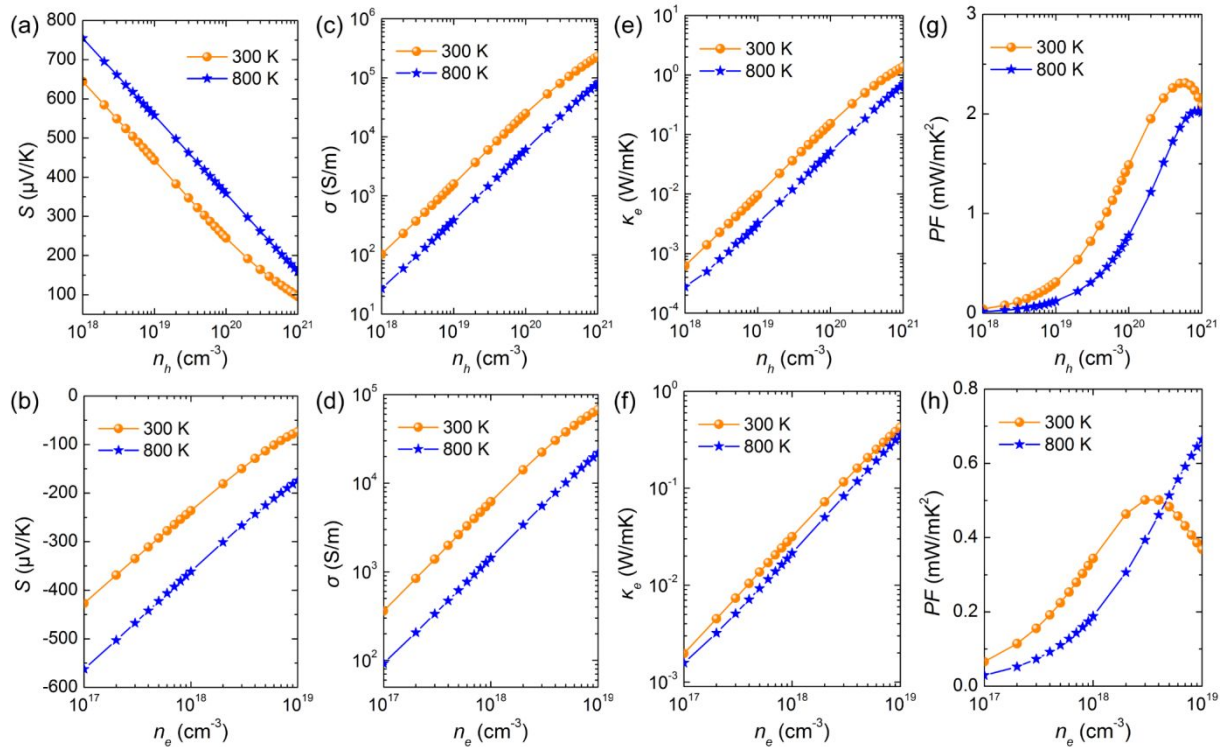


Figure 5. Electronic transport properties of CsK_2Sb . (a, b) Seebeck coefficient, (c, d) electrical conductivity, (e, f) electronic thermal conductivity, and (g, h) power factor as a function of hole and electron concentration.

The maximum room-temperature power factor for p -type CsK_2Sb is 2.3 mW/mK^2 , which is smaller than that of p -type Ba_2AuBi with a larger calculated value of 10 mW/mK^2 . The observed larger power factor in Ba_2AuBi is attributed to the “flat-and-dispersive” valence bands which are flat along one direction and highly dispersive along other directions. For n -type doping, the room-temperature power factor of CsK_2Sb tops out at 0.5 mW/mK^2 . This value is not only smaller than the theoretical results in full Heusler Ba_2AuBi (6 mW/mK^2)²⁴ and Sr_2BiAu (12 mW/mK^2)²⁶ but also lower than the experimental value in Fe_2VAl (2.5 mW/mK^2).⁵⁰ These relatively high power factors are mainly determined by the band structure. On the one hand,

according to $m^*_d = N_v^{2/3}m^*_b$, a large density of states effective mass m^*_d can be achieved in a band with large band degeneracy N_v and small band effective mass m^*_b . Therefore, increasing N_v is an effective route to improve the power factor despite of the small m^*_b . In CsK₂Sb, the CBM is located at the Γ point, which has the lowest valley degeneracy and low N_v . However, the CBM of Fe₂VAl, Ba₂AuBi, and Sr₂BiAu are away from the Γ point and thus significantly increasing N_v . On the other hand, the conduction band edges of Sr₂BiAu feature multiple energy-aligned low-effective-mass pockets, further pushing the power factor to a higher level. Although increasing the electron concentration can boost the n -type power factor of CsK₂Sb at 800 K, the corresponding ZT will be suppressed significantly at high electron concentration due to the rapid increase of electronic thermal conductivity. Therefore, the n -type ZT for the high temperature range tends to peak at a lower electron concentration than does the power factor.

Figure 6 displays the calculated ZT of CsK₂Sb as a function of carrier concentration at 300 K and 800 K. Both p - and n -type CsK₂Sb exhibit extraordinary thermoelectric performance at high temperatures. At 800 K, a peak p -type ZT value of 5.3 is achieved at the hole concentration of $2 \times 10^{20} \text{ cm}^{-3}$. For n -type doping, the highest ZT of 2.1 occurs at the electron concentration of $3 \times 10^{18} \text{ cm}^{-3}$. The lower ZT values for n -type doping than p -type doping are rooted in the higher electron thermal conductivity given that the n -type doping possesses relatively higher electron mobility. The higher ZT values for p -type doping than n -type doping are attributed to the high Seebeck coefficients originating from the flat valence band edges. On the other hand, the highest room-temperature ZT are 1.5 and 0.6 for p - and n -type CsK₂Sb, while the highest room-temperature ZT are 2.2 and 0.9 for p - and n -type CsK₂Bi (see Figure S11 in the Supporting Information). The room-temperature high-temperature p -type ZT of CsK₂Sb is comparable to the highest n -type ZT found in other full Heusler materials. The predicted p -type ZT values of CsK₂Bi and CsK₂Sb at room temperature and high temperature are comparable to the highest n -type ZT found in other full Heusler materials at the corresponding temperature range. Therefore, CsK₂Sb and CsK₂Bi are complements to the full Heusler compounds and could sever as p -type leg in thermoelectric devices targeting different temperature range.

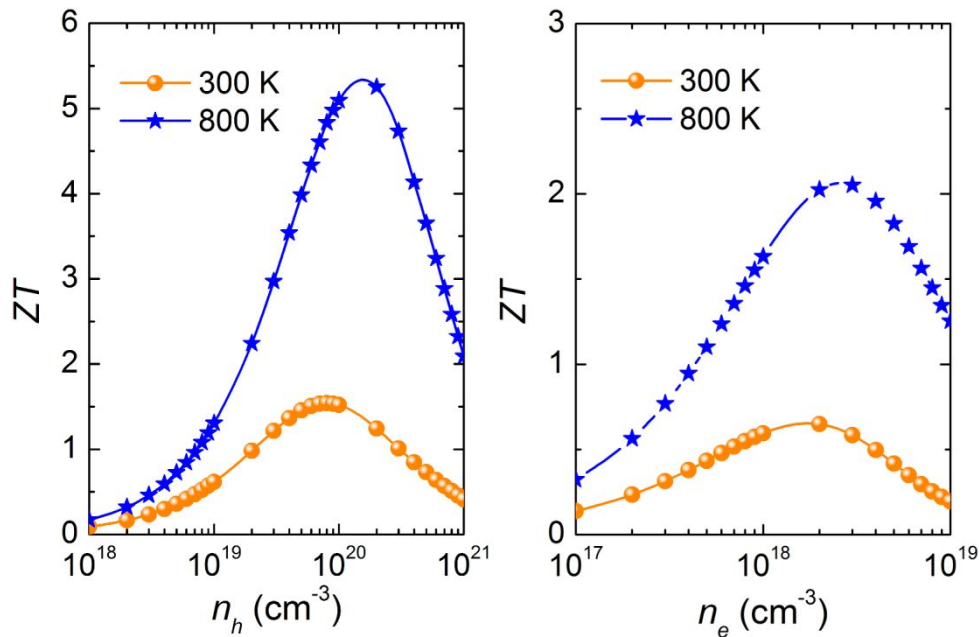


Figure 6. Calculated figure of merit of CsK₂Sb as a function of hole and electron concentration.

It should be noted that the extraordinary thermoelectric performance of CsK₂Sb and CsK₂Bi mainly arises from the ultralow lattice thermal conductivity due to the strong anharmonicity. To reveal the origin of such strong anharmonicity, we resort to the chemical bonding characteristics in CsK₂Sb and CsK₂Bi with the aid of the electron localization function (ELF) and the crystal orbital Hamilton population (COHP).^{51, 52} The ELF is a powerful tool to understand the bonding situations ranging from covalent to ionic bonds in a qualitative way, whose value is normalized between 0 and 1.^{11, 53} Higher ELF values concentrated in between two ions indicate strong covalent bonding, while low ELF values between the two ions are a signature of highly ionic bonds. As shown in Figure 7(a) and Figure S13(a), the electrons are bound very tightly to the atoms and there is no overlapping of charge clouds between each pair of atoms, indicating a strong ionic characteristic in these systems.

The COHP analysis is performed using the LOBSTER software⁵⁴ to reveal the bonding (stabilizing) and antibonding (destabilizing) contributions. Figure 7(b) and Figure S13(b) show the projected partial -COHP for different nearest-neighbor atomic pairs of CsK₂Sb and CsK₂Bi, and bonding states are positive and antibonding states are negative. It can be seen that all states are bonding for Sb/Bi-K interactions below the Fermi level. However, there are significant antibonding states for Cs-K, Cs-Sb, and Cs-Bi interactions in the valence band near the Fermi level. The presence of antibonding states below the Fermi level weakens the chemical bonding

and causes mutual repulsion between Cs atoms and neighboring K/Sb/Bi atoms, leading to larger ADP for Cs atoms. In addition, the peak COHP value of Cs-K antibonding in CsK_2Sb is a little higher than that in CsK_2Bi , which is consistent with the larger reduction of κ_L for CsK_2Sb when higher-order phonon interactions are included. Thus, it is likely that the antibonding-induced weak interactions between Cs atoms and neighboring K/Sb/Bi atoms trigger strong anharmonicity and lower the lattice thermal conductivity.

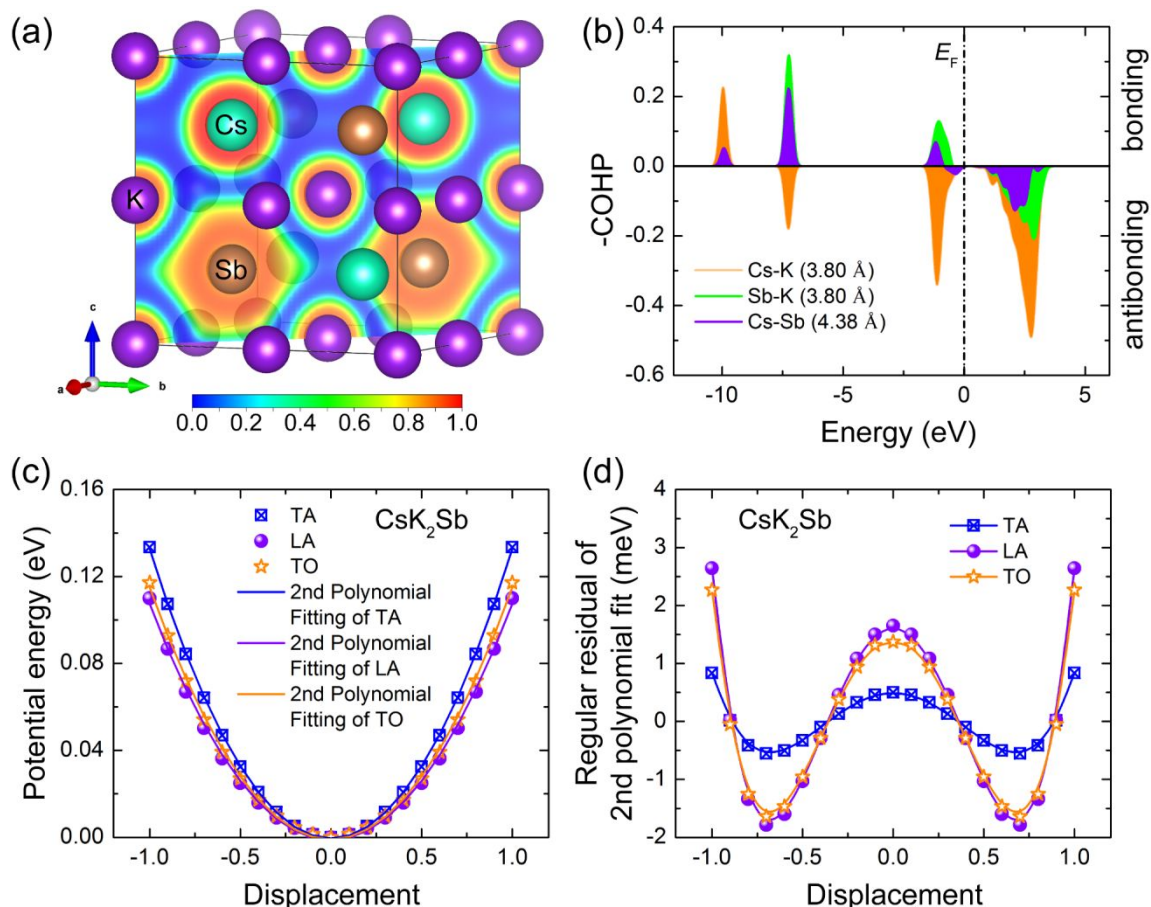


Figure 7. (a) Electron localization function of CsK_2Sb along the (110) plane of the conventional cell. (b) COHP projected on Cs-K, Sb-K, and Cs-Sb bonds. The bond length is included in the parenthesis. (c) Potential energy variation as a function of displacement for representative phonon modes of CsK_2Sb . (d) Regular residual analysis of the second polynomial fit to the potential energy curves.

In addition, the regular residual analysis is used to measure the quartic anharmonicity by calculating the potential energy versus the displacement perturbation for representative transverse acoustic (TA), longitudinal acoustic (LA), and transverse optical (TO) phonon modes at the X (0.5, 0.0, 0.5) point in the reciprocal space.⁵⁵ The potential energy curves of CsK_2Sb and CsK_2Bi are presented in Figure 7(c) and Figure S13(c), and the collective vibration vectors for the representative TA, LA, and TO phonon modes are shown in Figure S12. By

performing the second polynomial fitting to the potential energy curves, we show the corresponding regular residuals in Figure 7(d) and Figure S13(d). The displacement is scaled to the maximum amplitude of each normal mode. As suggested by Yue *et al.*,⁵⁵ the \sim/\sim -like and W/M -like residual shapes mean weak and strong quartic anharmonicity, respectively. We find that the shapes of residuals are all W -like, indicating the important role of quartic phonon anharmonicity in CsK₂Sb and CsK₂Bi.

4. CONCLUSION

In summary, we have investigated the thermal and electronic transport properties of full Heusler CsK₂X (X = Sb, Bi) based on first-principles calculations and machine learning potential. It is found that higher-order phonon interactions play an important role in suppressing phonon transport due to the coexistence of anharmonic rattling vibration of Cs atoms and low-frequency optical branches, which enhance the phonon anharmonicity and scattering channels, respectively. The inclusion of higher-order phonon interactions leads to a 40% reduction in κ_L compared to three-phonon scattering, resulting in ultralow κ_L of 0.14 and 0.13 W/mK in CsK₂Sb and CsK₂Bi at room temperature, which is the lowest κ_L among the known full Heusler materials. Through the analysis of the chemical bonding characteristics, we show that the underlying mechanism for the anharmonic rattling vibration of Cs atoms can be traced to the antibonding-induced weak interactions between Cs atoms and neighboring atoms. The strong fourth-order anharmonicity is also confirmed by the W -like residual shapes of potential energy variation. In the aspect of band structure, the flat and heavy valence band edges promote the density of states near the Fermi level and generate high p -type Seebeck coefficient, in contrast, the dispersive and light conduction band edges yield much larger n -type electrical conductivity and electronic thermal conductivity. Combining the ultralow lattice thermal conductivity and moderate Seebeck coefficient, unprecedentedly high $ZT = 2.2$ at 300 K and 5.3 at 800 K are achieved in p -type CsK₂Bi and CsK₂Sb. Our work unveils the dominant role of high-order phonon scattering for thermal insulation in full Heusler compounds and serves as a guide for further exploration of new high-performance thermoelectric materials.

Author information

Corresponding authors

*E-mail: zhangxiaoliang@dlut.edu.cn (X.Z.)

*E-mail: dwtang@dlut.edu.cn (D.T.)

*E-mail: hu@sc.edu (M.H.)

Conflicts of interest

The authors declare no competing financial interest.

Acknowledgments

The support from National Natural Science Foundation of China [51720105007, 52076031, and 52206219] and the Fundamental Research Funds for the Central Universities [DUT16RC(3)116], and the computing resources from Supercomputing Center of Dalian University of Technology, National Supercomputing Center in Shenzhen, and China National Grid (<http://www.cngrid.org>) / China Scientific Computing Grid (<http://www.scgrid.cn>)⁵⁶ are greatly acknowledged. Research reported in this publication was supported in part by the NSF (award number 2030128).

References

1. Mao, J.; Liu, Z.; Zhou, J.; Zhu, H.; Zhang, Q.; Chen, G.; Ren, Z., Advances in thermoelectrics. *Advances in Physics* 2018, 67, 69-147.
2. Sootsman, J. R.; Chung, D. Y.; Kanatzidis, M. G., New and old concepts in thermoelectric materials. *Angewandte Chemie International Edition* 2009, 48, 8616-8639.
3. Shi, X. L.; Zou, J.; Chen, Z. G., Advanced thermoelectric design: from materials and structures to devices. *Chemical Reviews* 2020, 120, 7399-7515.
4. Snyder, G. J.; Toberer, E. S., Complex thermoelectric materials. *Nature Materials* 2008, 7, 105-114.
5. Chang, C.; Zhao, L.-D., Anharmonicity and low thermal conductivity in thermoelectrics. *Materials Today Physics* 2018, 4, 50-57.
6. Wei, B.; Sun, Q.; Li, C.; Hong, J., Phonon anharmonicity: a pertinent review of recent progress and perspective. *SCIENCE CHINA Physics, Mechanics & Astronomy* 2021, 64, 117001.
7. Li, C. W.; Hong, J.; May, A. F.; Bansal, D.; Chi, S.; Hong, T.; Ehlers, G.; Delaire, O., Orbitally driven giant phonon anharmonicity in SnSe. *Nature Physics* 2015, 11, 1063-1069.
8. Nielsen, M. D.; Ozolins, V.; Heremans, J. P., Lone pair electrons minimize lattice thermal conductivity. *Energy & Environmental Science* 2013, 6, 570-578.
9. Jana, M. K.; Pal, K.; Waghmare, U. V.; Biswas, K., The origin of ultralow thermal conductivity in InTe: lone-pair-induced anharmonic rattling. *Angewandte Chemie International Edition* 2016, 55, 7792-7796.
10. Lee, S.; Esfarjani, K.; Luo, T. F.; Zhou, J. W.; Tian, Z. T.; Chen, G., Resonant bonding leads to low

lattice thermal conductivity. *Nature Communications* 2014, 5, 3525.

11. Qin, G.; Zhang, X.; Yue, S.-Y.; Qin, Z.; Wang, H.; Han, Y.; Hu, M., Resonant bonding driven giant phonon anharmonicity and low thermal conductivity of phosphorene. *Physical Review B* 2016, 94, 165445.
12. Pal, K.; Xia, Y.; He, J.; Wolverton, C., Intrinsically low lattice thermal conductivity derived from rattler cations in an AMM'Q₃ family of chalcogenides. *Chemistry of Materials* 2019, 31, 8734-8741.
13. Jana, M. K.; Pal, K.; Warankar, A.; Mandal, P.; Waghmare, U. V.; Biswas, K., Intrinsic rattler-induced low thermal conductivity in zintl type TlInTe₂. *Journal of the American Chemical Society* 2017, 139, 4350-4353.
14. Li, J.; Hu, W.; Yang, J., High-throughput screening of rattling-induced ultralow lattice thermal conductivity in semiconductors. *Journal of the American Chemical Society* 2022, 144, 4448-4456.
15. Takabatake, T.; Suekuni, K.; Nakayama, T.; Kaneshita, E., Phonon-glass electron-crystal thermoelectric clathrates: Experiments and theory. *Reviews of Modern Physics* 2014, 86, 669-716.
16. Tadano, T.; Tsuneyuki, S., Quartic anharmonicity of rattlers and its effect on lattice thermal conductivity of clathrates from first principles. *Physical Review Letters* 2018, 120, 105901.
17. Shi, X.; Yang, J.; Salvador, J. R.; Chi, M.; Cho, J. Y.; Wang, H.; Bai, S.; Yang, J.; Zhang, W.; Chen, L., Multiple-filled skutterudites: high thermoelectric figure of merit through separately optimizing electrical and thermal transports. *Journal of the American Chemical Society* 2011, 133, 7837-7846.
18. Li, W.; Mingo, N., Ultralow lattice thermal conductivity of the fully filled skutterudite YbFe₄Sb₁₂ due to the flat avoided-crossing filler modes. *Physical Review B* 2015, 91, 144304.
19. Liu, Z.; Zhang, W.; Gao, W.; Mori, T., A material catalogue with glass-like thermal conductivity mediated by crystallographic occupancy for thermoelectric application. *Energy & Environmental Science* 2021, 14, 3579-3587.
20. Mukhopadhyay, S.; Parker David, S.; Sales Brian, C.; Puzos Alexander, A.; McGuire Michael, A.; Lindsay, L., Two-channel model for ultralow thermal conductivity of crystalline Tl₃VSe₄. *Science* 2018, 360, 1455-1458.
21. Xia, Y.; Ozoliņš, V.; Wolverton, C., Microscopic mechanisms of glasslike lattice thermal transport in cubic Cu₁₂Sb₄S₁₃ tetrahedrites. *Physical Review Letters* 2020, 125, 085901.
22. Tan, G.; Hao, S.; Zhao, J.; Wolverton, C.; Kanatzidis, M. G., High thermoelectric performance in electron-doped AgBi₃S₅ with ultralow thermal conductivity. *Journal of the American Chemical Society* 2017, 139, 6467-6473.
23. He, J.; Amsler, M.; Xia, Y.; Naghavi, S. S.; Hegde, V. I.; Hao, S.; Goedecker, S.; Ozoliņš, V.; Wolverton, C., Ultralow thermal conductivity in full heusler semiconductors. *Physical Review Letters* 2016, 117, 046602.
24. Park, J.; Xia, Y.; Ozoliņš, V., High thermoelectric power factor and efficiency from a highly dispersive band in Ba₂BiAu. *Physical Review Applied* 2019, 11, 014058.
25. Ma, J.; Nissimagoudar, A. S.; Wang, S.; Li, W., High thermoelectric figure of merit of full-Heusler Ba₂AuX (X = As, Sb, and Bi). *physica status solidi (RRL) – Rapid Research Letters* 2020, 14, 2000084.
26. Park, J.; Xia, Y.; Ganose, A. M.; Jain, A.; Ozoliņš, V., High thermoelectric performance and defect energetics of multipocketed full Heusler compounds. *Physical Review Applied* 2020, 14, 024064.
27. Kresse, G.; Furthmüller, J., Efficient iterative schemes for ab initio total-energy calculations using a plane-wave basis set. *Physical Review B* 1996, 54, 11169-11186.
28. Kresse, G.; Joubert, D., From ultrasoft pseudopotentials to the projector augmented-wave method. *Physical Review B* 1999, 59, 1758-1775.
29. Perdew, J. P.; Burke, K.; Ernzerhof, M., Generalized gradient approximation made simple. *Physical Review Letters* 1996, 77, 3865-3868.
30. Shapeev, A. V., Moment tensor potentials: a class of systematically improvable interatomic potentials. *Multiscale Modeling & Simulation* 2016, 14, 1153-1173.

31. Plimpton, S., Fast parallel algorithms for short-range molecular dynamics. *Journal of Computational Physics* 1995, 117, 1-19.
32. Eriksson, F.; Fransson, E.; Erhart, P., The Hiphive package for the extraction of high-order force constants by machine learning. *Advanced Theory and Simulations* 2019, 2, 1800184.
33. Li, W.; Carrete, J.; A. Katcho, N.; Mingo, N., ShengBTE: a solver of the Boltzmann transport equation for phonons. *Computer Physics Communications* 2014, 185, 1747-1758.
34. Gao, Y.; Zhang, X.; Jing, Y.; Hu, M., The unexpected non-monotonic inter-layer bonding dependence of the thermal conductivity of bilayered boron nitride. *Nanoscale* 2015, 7, 7143-7150.
35. Larkin, J.; Turney, J.; Massicotte, A.; Amon, C.; McGaughey, A., Comparison and evaluation of spectral energy methods for predicting phonon properties. *Journal of Computational and Theoretical Nanoscience* 2014, 11, 249-256.
36. Thomas, J. A.; Turney, J. E.; Iutzi, R. M.; Amon, C. H.; McGaughey, A. J. H., Predicting phonon dispersion relations and lifetimes from the spectral energy density. *Physical Review B* 2010, 81, 081411.
37. Ganose, A. M.; Park, J.; Faghaninia, A.; Woods-Robinson, R.; Persson, K. A.; Jain, A., Efficient calculation of carrier scattering rates from first principles. *Nature communications* 2021, 12, 2222.
38. Cocchi, C.; Mistry, S.; Schmeißer, M.; Amador, R.; Kühn, J.; Kamps, T., Electronic structure and core electron fingerprints of caesium-based multi-alkali antimonides for ultra-bright electron sources. *Scientific Reports* 2019, 9, 18276.
39. Cocchi, C.; Mistry, S.; Schmeißer, M.; Kühn, J.; Kamps, T., First-principles many-body study of the electronic and optical properties of CsK₂Sb, a semiconducting material for ultra-bright electron sources. *Journal of Physics: Condensed Matter* 2018, 31, 014002.
40. Khan, Z.; Murtaza, G.; Khan, A. A.; Laref, A.; Kattan, N. A.; Haneef, M., Different physical properties of bi-alkali pnictogen compounds using density functional theory. *International Journal of Energy Research* 2021, 45, 7703-7718.
41. Maughan, A. E.; Paecklar, A. A.; Neilson, J. R., Bond valences and anharmonicity in vacancy-ordered double perovskite halides. *Journal of Materials Chemistry C* 2018, 6, 12095-12104.
42. Bhui, A.; Ghosh, T.; Pal, K.; Singh Rana, K.; Kundu, K.; Soni, A.; Biswas, K., Intrinsically low thermal conductivity in the n-type vacancy-ordered double perovskite Cs₂SnI₆: octahedral rotation and anharmonic rattling. *Chemistry of Materials* 2022, 34, 3301-3310.
43. Jong, U.-G.; Kim, Y.-S.; Ri, C.-H.; Kye, Y.-H.; Pak, C.-J.; Cottenier, S.; Yu, C.-J., Twofold rattling mode-induced ultralow thermal conductivity in vacancy-ordered double perovskite Cs₂SnI₆. *Chemical Communications* 2022, 58, 4223-4226.
44. Lin, W.; He, J.; Su, X.; Zhang, X.; Xia, Y.; Bailey, T. P.; Stoumpos, C. C.; Tan, G.; Rettie, A. J. E.; Chung, D. Y.; Dravid, V. P.; Uher, C.; Wolverton, C.; Kanatzidis, M. G., Ultralow thermal conductivity, multiband electronic structure and high thermoelectric figure of merit in TlCuSe. *Advanced Materials* 2021, 33, 2104908.
45. Ghosh, C.; Varma, B. P., Preparation and study of properties of a few alkali antimonide photocathodes. *Journal of Applied Physics* 1978, 49, 4549-4553.
46. Frost, J. M., Calculating polaron mobility in halide perovskites. *Physical Review B* 2017, 96, 195202.
47. Jung, Y.-K.; Han, I. T.; Kim, Y. C.; Walsh, A., Prediction of high thermoelectric performance in the low-dimensional metal halide Cs₃Cu₂I₅. *npj Computational Materials* 2021, 7, 51.
48. Spooner, K. B.; Ganose, A. M.; Leung, W. W. W.; Buckeridge, J.; Williamson, B. A. D.; Palgrave, R. G.; Scanlon, D. O., BaBi₂O₆: a promising n-type thermoelectric oxide with the PbSb₂O₆ crystal structure. *Chemistry of Materials* 2021, 33, 7441-7456.
49. Verdi, C.; Caruso, F.; Giustino, F., Origin of the crossover from polarons to Fermi liquids in transition metal oxides. *Nature Communications* 2017, 8, 15769.

50. Bilec, D. I.; Hautier, G.; Waroquiers, D.; Rignanese, G.-M.; Ghosez, P., Low-dimensional transport and large thermoelectric power factors in bulk semiconductors by band engineering of highly directional electronic states. *Physical Review Letters* 2015, 114, 136601.
51. Dronskowski, R.; Bloechl, P. E., Crystal orbital Hamilton populations (COHP): energy-resolved visualization of chemical bonding in solids based on density-functional calculations. *The Journal of Physical Chemistry* 1993, 97, 8617-8624.
52. Deringer, V. L.; Tchougréeff, A. L.; Dronskowski, R., Crystal orbital Hamilton population (COHP) analysis as projected from plane-wave basis sets. *The Journal of Physical Chemistry A* 2011, 115, 5461-5466.
53. Qin, G.; Qin, Z.; Wang, H.; Hu, M., Lone-pair electrons induced anomalous enhancement of thermal transport in strained planar two-dimensional materials. *Nano Energy* 2018, 50, 425-430.
54. Nelson, R.; Ertural, C.; George, J.; Deringer, V. L.; Hautier, G.; Dronskowski, R., LOBSTER: Local orbital projections, atomic charges, and chemical-bonding analysis from projector-augmented-wave-based density-functional theory. *Journal of Computational Chemistry* 2020, 41, 1931-1940.
55. Yue, S.-Y.; Zhang, X.; Qin, G.; Phillpot, S. R.; Hu, M., Metric for strong intrinsic fourth-order phonon anharmonicity. *Physical Review B* 2017, 95, 195203.
56. Xiao, H., Wu, H., Chi, X., SCE: grid environment for scientific computing, in *Networks for Grid Applications, GridNets 2008*. Lecture Notes of the Institute for Computer Sciences, Social Informatics and Telecommunications Engineering, vol 2. Springer, Berlin, Heidelberg, 2009.